(Received 17 March 2026, Accepted 13 April 2026, Scheduled 1 May 2026)

Surface Wave Couplers for Terahertz Wireless Communication Receiver Front Ends

Yanfeng Zhao[1,#], Jiajun He[1,#], Cong Liu[1], Xiaoyuan Hao[2], Xizhi Li[1], Wei Wu[1], Quan Xu[1,*], Xueqian Zhang[1,*], and Jiaguang Han[1,2,*]

[1] *Center for Terahertz Waves, College of Precision Instrument and Optoelectronics Engineering Tianjin University, Tianjin 300072, China*
[2] *Guangxi Key Laboratory of Optoelectronic Information Processing, School of Optoelectronic Engineering Guilin University of Electronic Technology, Guilin 541004, China*

ABSTRACT: Free-space electromagnetic waves can be coupled into on-chip propagating surface waves (SWs), a process that holds great promise for receiver front ends in wireless communication systems. However, it has traditionally faced challenges in terms of coupling efficiency and controlling the on-chip wavefront of SWs. To address these challenges, we designed and experimentally demonstrated SW couplers operating in the terahertz regime based on metal-insulator-metal resonators. Our devices achieve not only broadband and highly efficient coupling, with an efficiency exceeding 60% over a 20 GHz bandwidth, but also enable the directional steering of the excited SWs to designated on-chip ports. Thus, mode conversion and on-chip routing functionalities are seamlessly integrated into a single compact component. Based on this design, we fabricated devices and implemented corresponding terahertz wireless communication links, successfully demonstrating 16-QAM data transmission in both single-link and dual-link configurations.

1. INTRODUCTION

Terahertz waves offer enormous bandwidth capable of supporting single-link communication rates ranging from tens to hundreds of Gbit/s, making them a key for next-generation (6G) and future wireless communication systems (XG) [1–3]. Significant progress has been made in the development of terahertz communication devices, including on-chip terahertz waveguides, signal-processing components, and transmitter front-end antennas, enabled by advances in effective refractive index engineering [4–8], valley-topological photonic crystals [9–15], and inverse design methodologies [16, 17]. At the receiver front end, coupling free-space terahertz waves into surface waves (SWs) is highly advantageous: SWs not only serve as efficient on-chip carriers for signal transmission but also enhance light-matter interactions through their plasmonic nature [18–20], thereby facilitating seamless integration of terahertz wireless links with on-chip processing units for subsequent information handling [21–23]. Conventional approaches to achieve wavevector matching between free-space terahertz waves and SWs typically rely on bulky components, such as prisms or gratings, which suffer from large footprints and limited functional versatility.

Recently, metasurfaces have emerged as an ideal platform for both wavefront manipulation in free space [24, 25] and the coupling and manipulation of SWs [26–28]. This versatility stems from local control that their constituent meta-atoms provide over the phase, amplitude, polarization, and dispersion of electromagnetic fields through engineered resonances. A variety of SW couplers have been realized using metasurfaces, including directional couplers [29–31], SW lenses [32], and plasmonic vortex generators [33–35]. In particular, leveraging the geometric phase concept, meta-atoms functioning as SW dipole sources have served as simple yet powerful building blocks for tailored SW beam launching and complex wavefront generation [36, 37]. However, in this approach, each meta-atom acts as a subwavelength half-wave plate under circularly polarized incidence, and only half of the incident power couples to the SW dipole mode, fundamentally limiting the device efficiency to below 50% [28, 36–38]. In contrast, Liu et al. demonstrated highly efficient SW coupling by employing subwavelength quarter-wave plates as meta-atoms, which can, in principle, fully harness the incident circularly polarized field and surpass the 50% efficiency barrier [38]. Nevertheless, this strategy provides only limited wavefront engineering capabilities. In essence, current SW couplers face an intrinsic trade-off between coupling efficiency and on-chip manipulability, and none have yet been integrated into practical wireless receiver front ends.

To address this issue, we propose a metasurface coupler based on subwavelength quarter-wave plate meta-atoms engineered to exploit both the geometric and resonant phases for full-field manipulation. As illustrated in Fig. 1(a), an incident wave from a horn antenna is coupled into the focused SWs and subsequently guided into a metallic waveguide by an adiabatic coupler. Full-wave simulations predicted a coupling efficiency exceeding 60% over a 20 GHz bandwidth near 0.14 THz. We further perform a numerical analysis of the SW excitation by meta-atoms, revealing that their dipole response can be decomposed into two equal-weight components. By independently

* Corresponding authors: Quan Xu (quanxu@tju.edu.cn); Xueqian Zhang (alearn1988@tju.edu.cn); Jiaguang Han (jiaghan@tju.edu.cn).
# These authors contributed equally to this work.

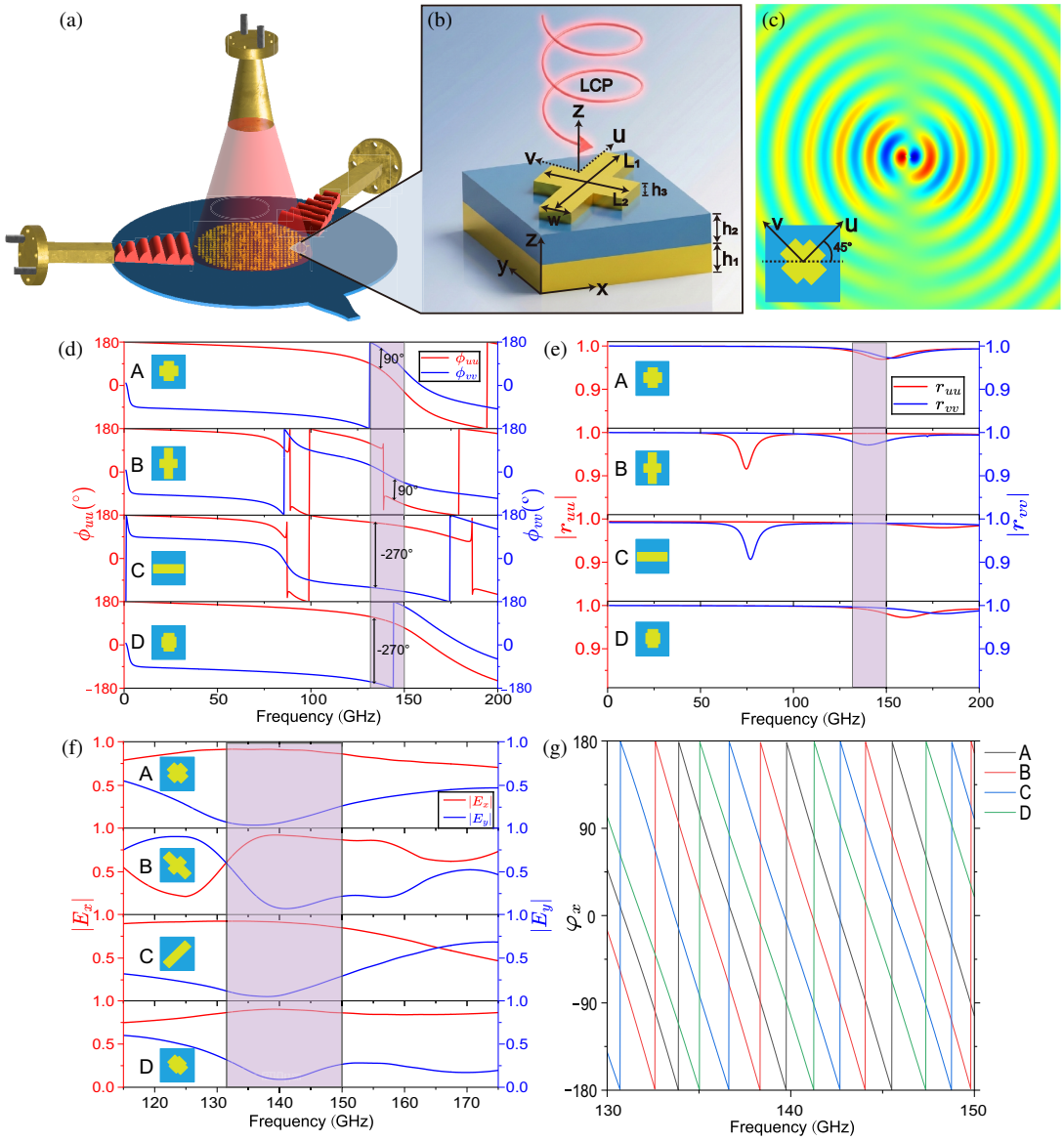

FIGURE 1. Device principle and electromagnetic response of the selected meta-atoms. (a) Schematic illustration of the SW couplers. (b) Schematic of the meta-atom. L_1 and L_2 are the arm lengths along the u- and v-directions. (c) The simulated E_z-field distribution at 0.14 THz. (d) Simulated phase retardation $\Delta\varphi$ between the two orthogonal axes. (e) Reflection amplitudes (r_{uu} and r_{vv}) of the four selected unit cells. (f) Polarization conversion performance under LCP incidence after rotating the structures by 45°. (g) Resonant phase distributions of the four meta-atoms (A-D).

tailoring the geometric and resonant phases of the meta-atoms, these components can be controlled at will, enabling the high-degree-of-freedom synthesis of complex SW wavefronts. The fabricated devices demonstrated on-chip SW focusing with single and dual focal points, and were successfully integrated into terahertz wireless links that achieve error-free 16-QAM transmission in both single-link and dual-link configurations. These results establish the proposed coupler as a high-efficiency, multifunctional receiver front end suitable for practical terahertz communication systems.

2. RESULTS

This section details the meta-atom design, followed by the design and experimental characterization of the unidirectional and functional SW couplers.

2.1. Design of the Meta-atom

We began by designing efficient reflective meta-atoms operating as quarter-wave plates in the terahertz band. The optical properties of these structures are characterized by a reflection matrix derived through a sequence of coordinate and basis transformations of

$$R = A\mathrm{e}^{\mathrm{i}\left(\varphi+\frac{\pi}{4}\right)}\begin{bmatrix} \cos\frac{\Delta\varphi}{2} & -\mathrm{i}\mathrm{e}^{-\mathrm{i}2\theta}\sin\frac{\Delta\varphi}{2} \\ -\mathrm{i}\mathrm{e}^{\mathrm{i}2\theta}\sin\frac{\Delta\varphi}{2} & \cos\frac{\Delta\varphi}{2} \end{bmatrix}.$$

Here, A and $\varphi = \frac{\varphi_{uu}+\varphi_{vv}}{2} - \frac{\pi}{4}$ denote the reflection amplitude and resonance phase, respectively, while θ represents the orientation angle, and $\Delta\varphi = \varphi_{vv} - \varphi_{uu}$. Considering the specific condition $\Delta\varphi = \frac{\pi}{2}$, the resonance phase φ can be derived as $\varphi = \frac{\varphi_{uu}+\varphi_{vv}}{2} - \frac{\pi}{4} = \varphi_{xx} - \frac{\pi}{4}$. Upon the incidence of a

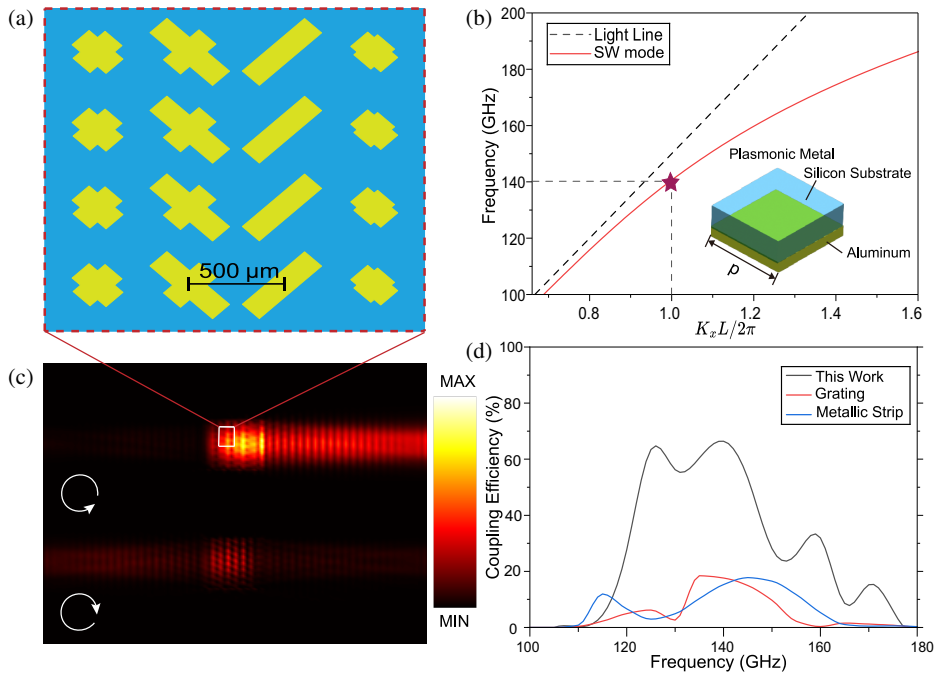

FIGURE 2. Simulation verification of the SW coupler. (a) Schematic of the super-cell arrangement. (b) SW dispersion relation. Red and black dashed lines denote the SW mode and vacuum light line, respectively, with the star marking the mode at 0.14 THz. (c) Simulated near-field distributions under LCP and RCP incidences. (d) Coupling efficiency comparison of the proposed SW coupler (black), the conventional grating coupler (red), and the geometric phase metallic strip coupler (blue).

circularly polarized wave $E_{\text{in}} = \frac{\sqrt{2}}{2}\begin{bmatrix} 1 \\ i\sigma \end{bmatrix}$ with $\sigma \in \{+,-\}$ corresponding to the left- or right-handed circular polarizations (LCP or RCP), the reflected wave can be expressed as [38]:

$$E_r = \text{SRE}_{\text{in}} = Ae^{\text{i}(\varphi+\sigma\theta)}\left[\cos\left(\sigma\theta - \frac{\pi}{4}\right)\hat{\mathbf{x}} + \sin\left(\sigma\theta - \frac{\pi}{4}\right)\hat{\mathbf{y}}\right]. \quad (1)$$

Here, $S = \frac{\sqrt{2}}{2}\begin{bmatrix} 1 & 1 \\ i & -i \end{bmatrix}$ represents the transformation matrix from the circular polarization basis to the linear polarization basis. Observation from Eq. (1) reveals that for LCP incidence with $\theta = \pi/4$, the reflected wave is linearly polarized along the x-direction. Guided by this theory, we selected a set of cross-shaped structures shown in Fig. 1(b) via parameter sweeps. The linewidth was fixed at $W = 130\,\mu\text{m}$. The optimized device architecture comprises a silicon substrate with a thickness of 100 μm, backed by a 200 nm aluminum (Al) ground plane. This sub-wavelength thickness, being significantly below the $\lambda_0/2n$ threshold required for the fundamental Fabry-Perot mode, ensures the suppression of parasitic substrate resonances. On the top surface, Al cross-shaped resonators with a thickness of 200 nm are patterned. By optimizing the arm lengths L_1 and L_2, four specific meta-atoms were selected: A ($L_1 = 245\,\mu\text{m}$, $L_2 = 260\,\mu\text{m}$), B ($L_1 = 272\,\mu\text{m}$, $L_2 = 480\,\mu\text{m}$), C ($L_1 = 477\,\mu\text{m}$, $L_2 = 130\,\mu\text{m}$), and D ($L_1 = 182\,\mu\text{m}$, $L_2 = 230\,\mu\text{m}$). Simulations of these unit cells reveal that the resonators function as sub-wavelength dipole sources under LCP illumination (Fig. 1(c)). As shown in Figs. 1(d) and 1(e), these structures exhibit a stable phase retardation $\Delta\varphi \approx \pi/2$ and high reflection amplitudes ($r_{uu}, r_{vv} > 0.9$) across the 0.13–0.15 THz frequency band, confirming an excellent quarter-wave plate response.

After rotating the structures by 45°, we evaluated their electromagnetic responses via time-domain simulations. Fig. 1(f) verifies their polarization conversion properties, showing that $|E_x|$ is significantly larger than $|E_y|$ within the target band of 0.13–0.15 THz. Meanwhile, as depicted in Fig. 1(g), the four selected meta-atoms provide discrete phase steps of roughly $-\pi/2$ covering the full 0–2π range.

2.2. High-Efficiency SW Coupler

To verify the high efficiency of the aforementioned meta-atoms, four types of meta-atoms (A-D) are arranged with a phase gradient of $-\pi/2$ to construct a unidirectional SW coupler. As illustrated in Fig. 2(a), the orientation angles of these meta-atoms are all fixed at 45°, and they are arranged periodically with a period p. The meta-atom period p was determined via rigorous momentum matching. This step ensures surface mode propagation and minimizes dissipation caused by momentum mismatch. Fig. 2(b) depicts the dispersion relation of the SW mode supported by the silicon-aluminum interface. At 0.14 THz, the SW wavevector is $k_{\text{sw}} \approx 1.07k_0$ (where k_0 is the wavevector in vacuum). Consequently, the phase gradient of the metasurface is set to $\zeta = 2\pi/L = 2\pi/0.93\lambda_0$, where $L = 0.93\lambda_0 = 2000\,\mu\text{m}$ represents the lattice constant of the super-cell. Since each super-cell consists of four meta-atoms. Therefore, the period p of the individual meta-atom is

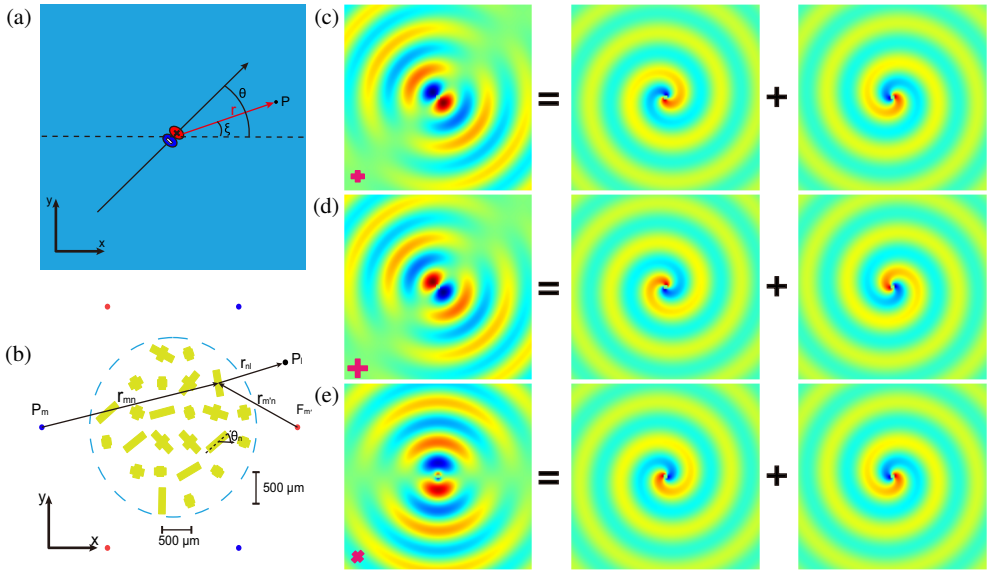

FIGURE 3. Schematic illustration of the working principle for the cross-shaped resonators. (a) SW excitation generated by an ideal dipole source. (b) Schematic of the proposed holographic design scheme. (c)–(e) Calculated SW field distributions and their corresponding components under LCP incidence. The results correspond to three representative resonators defined by (c) $\theta = 0$, $\varphi = 0$; (d) $\theta = 0$, $\varphi = \pi$; and (e) $\theta = \pi/4$, $\varphi = 0$.

calculated as $p = L/4 = 500\,\mu\text{m}$. Under LCP and RCP incidence, this device exhibits the following phase distribution of $\Phi_L = \Phi_0 - \zeta x$ and $\Phi_R = \Phi - \zeta x - \pi/2$. The surface wave vector k_{sw} supported by the plasmonic metal matches the phase gradient of the meta-atoms under LCP illumination. Consequently, the SW coupler efficiently converts the incident waves into rightward-propagating SWs, as depicted in Fig. 2(c). Conversely, under RCP incidence, the meta-atoms convert the incident wave to linear polarization along the y direction, as dictated by Eq. (1). The resulting polarization and momentum mismatch subsequently suppress the SW excitations.

As shown in Fig. 2(d), the proposed unidirectional SW coupler achieves a coupling efficiency of 66.5% (see Supplementary Note 1 for calculation details). This value excludes reflection and scattering losses, while incorporating both metallic absorption (10%, as detailed in Supplementary Note 1) and dielectric dissipation (0.5%). Such losses could be further mitigated by employing low-loss materials, such as Ag or Au. In addition, owing to the intrinsic resonance of the meta-atoms, a degree of momentum mismatch persists between the incident wave and the target modes. This leads to surface waves in non-target directions, thereby constituting a primary factor in the observed reduction of coupling efficiency. This performance stands in sharp contrast to the geometric phase metallic strip couplers and the conventional grating couplers (shown in Supplementary Note 1, Figs. S2(a) and S2(b), respectively), which exhibit efficiencies of only 15% and 17%, respectively. Consequently, our design delivers a ∼4-fold enhancement over these benchmarks, effectively overcoming the longstanding efficiency bottleneck. To further optimize performance, a dielectric overlayer (e.g., polyimide) can be integrated to enhance surface wave confinement by increasing the local refractive index. Moreover, such a layer serves to mitigate reflection losses by smoothing the impedance transition between the air and the high-index silicon substrate.

2.3. Dipolar SW Excitations and Near-Field Holography

Theoretically, a dipole source can be modeled as a pair of monopole sources with equal intensity but opposite phases, separated by a subwavelength distance. Consider a dipole source located in the *xy*-plane, as shown in Fig. 3(a). This dipole is excited only by the polarization component aligned with its orientation, thereby generating surrounding SWs. To model the physical response of the cross-shaped resonator, we treat it as a superposition of two orthogonal metallic strip resonators along the u and v directions. In this case, the SW excitation of the cross-shaped resonator can be seen as the superposition of two orthogonal dipole sources, which behave like a single dipole source approximately along the 45° direction in the *uv* coordinate system. The SW excitation of a single meta-atom can be described as (see Supplementary Note 2 for the full derivation):

$$E_P = \sqrt{2}\eta \exp\left(\mathrm{i}k_{\text{sw}}|r|\right) \cdot \frac{\exp\left[\mathrm{i}\left(\varphi + 2\sigma\theta - \sigma\xi - \frac{\pi}{4}\right)\right] + \exp\left[\mathrm{i}\left(\varphi + \sigma\xi + \frac{\pi}{4}\right)\right]}{\mathrm{i}\sqrt{\lambda_{\text{sw}}|r|}}. \quad (2)$$

Here, η is the complex coefficient describing the SW excitation efficiency; r is the vector pointing from the dipole source to point P; ξ denotes the angle between r and the x-axis.

Equation (2) characterizes the SW excitation field of the cross-shaped resonator under a circularly polarized incidence. Figs. 3(c)–(e) present the radiated field distributions for three distinct configurations: ($\theta = 0$, $\varphi = 0$), ($\theta = 0$, $\varphi = \pi$), ($\theta = \pi/4$, $\varphi = 0$), where θ represents the orientation angle of the resonator. By decomposing the total field, we revealed that the excitation originated from two distinct constituent terms, both manifesting as swirl fields with opposite helicities. Term 1 is modulated by both the resonant phase φ and the geometric rotation angle θ, while exhibiting a spin dependence of 2σ. In contrast, Term 2 depends exclusively on the resonant phase φ.

Notably, both terms share an additional phase factor of $\sigma\xi+\pi/4$. This distinctive excitation behavior is attributed to the spin-orbit coupling effect [39–41]. The coherent interference between these two terms dictates the final SW excitation response, providing a robust mechanism for arbitrary wavefront shaping by independently tuning the resonant and geometric degrees of freedom.

Leveraging the unique SW excitation effects of cross-shaped resonators, we integrated near-field holographic algorithms to achieve the flexible manipulation of SW wavefronts. As illustrated in Fig. 3(b), consider N dipole sources (depicted as yellow cross-shaped resonators) distributed within a circular region with radius R. These sources are arranged with a period p along both the x- and y-axes, constituting a hologram that dictates the near-field energy distribution. We define m virtual focal points located outside the circular region, denoted as P_m. Based on the principle of optical reversibility, these virtual focal points are treated as point sources with a wavelength of λ_{sw}. Consequently, the field superposition at the position of the nth dipole source is calculated as:

$$H_n = \sum_m \frac{C_m \exp\left(-\mathrm{i}\sigma \arg(r_{mn}) - \mathrm{i}k_{\mathrm{sw}}|r_{mn}|\right)}{\mathrm{i}\sqrt{\lambda_{\mathrm{sw}}|r_{mn}|}}. \quad (3)$$

Here, C_m denotes the complex coefficient of the mth virtual focal point P_m, and r_{mn} represents the vector pointing from P_m (indicated by the blue dot) to the nth dipole source. By combining Eq. (3) with the second term of Eq. (2), the required resonant phase for each dipole source is derived as:

$$\varphi_n = -\arg(H_n) + \frac{\pi}{4}. \quad (4)$$

To implement the prescribed focusing function, cross-shaped resonators are arranged at each unit cell with the required resonant phase φ_n governed by Eq. (4). Furthermore, we define m' additional virtual focal points at $F_{m'}$ (indicated by the red dots). Similarly, the superposition effect of these points at the location of the nth dipole source is calculated as:

$$H'_n = \sum_{m'} \frac{C_{m'} \exp\left(-\mathrm{i}\sigma \arg(r_{m'n}) - \mathrm{i}k_{\mathrm{sw}}|r_{m'n}|\right)}{\mathrm{i}\sqrt{\lambda_{\mathrm{sw}}|r_{m'n}|}}. \quad (5)$$

Here, C'_m denotes the complex coefficient of the m'th virtual focal point $F_{m'}$, and $r_{m'n}$ represents the vector pointing from $F_{m'}$ to the nth dipole source. Integrating Eq. (5) with the first term of Eq. (2), the required orientation angle θ_n for each unit cell can be calculated as:

$$\theta_n = \frac{\arg(H'_n) + \varphi_n + \frac{\pi}{4}}{2}. \quad (6)$$

At this point, the resonance phase (Eq. (4)) and geometric phase (Eq. (6)) for each unit cell location have been fully determined. The final design is realized by arranging meta-atoms of specific geometric parameters and rotating them by the corresponding angles, to satisfy the required phase profile. Finally, the total SW field at an arbitrary point P_l, formed by the superposition of all dipole sources, is given by:

$$E_l = \sum_n \eta\sqrt{2}\exp\left(\mathrm{i}k_{\mathrm{sw}}|r_{nl}|\right) \cdot \frac{\exp\left[\mathrm{i}\left(\arg(r_{nl}) + \varphi_n + \frac{\pi}{4}\right)\right] + \exp\left[\mathrm{i}\left(\varphi_n - 2\theta_n - \arg(r_{nl}) - \frac{\pi}{4}\right)\right]}{\mathrm{i}\sqrt{\lambda_{\mathrm{sw}}|r_{nl}|}}. \quad (7)$$

Here, r_{nl} denotes the vector pointing from the center of the nth dipole source to the observation point P_l (indicated by the black dot). Eq. (7) characterizes the SW excitation field under LCP incidence.

2.4. Functional SW Couplers

To verify the flexibility of this approach for SW wavefront manipulation, we designed three representative devices (D1–D3) operating in the 0.13–0.15 THz band. The resonators are periodically arranged with a subwavelength period of 500 μm along both the x- and y-axes, covering a circular region of radius 7.50 mm, centered at the origin (0, 0).

Specifically, all three devices were designed to generate focal spots on a circumference with a radius of 25 mm. D1 implements single-point focusing by solely utilizing the resonance phase φ_n. For the quantitative analysis, two observation ports were positioned at coordinates $(-25.00, 0.00)$ mm (Port 1) and (25.00, 0.00) mm (Port 2). In contrast, D2 and D3 exploit the synergy between the resonance phase φ_n and the geometric phase θ_n to achieve dual-point focusing. For D2, dual-point focusing is realized with a 180° angular separation between Port 1 at $(-25.00, 0.00)$ mm and Port 2 at (25.00, 0.00) mm. For D3, three ports are distributed with 120° angular spacing to characterize the output performance. Port 1 was fixed at $(-25.00, 0.00)$ mm, whereas Port 2 and Port 3 were symmetrically placed at (12.50, 21.65) mm and (12.50, -21.65) mm. This three-port configuration facilitates a comprehensive evaluation of both power transmission and inter-port isolation.

Figure 4 presents a comparative analysis of the SW electric field distributions under LCP excitation. The full-wave simulations (Figs. 4(d)–(f)) exhibit remarkable agreement with the theoretical predictions in Figs. 4(a)–(c). To quantitatively evaluate the device performance, we calculated the coupling efficiency by integrating the power flux across a predefined cross-section at the focal plane, following the methodology described in Supplementary Note 1. As shown in Figs. 4(g)–(i), the total coupling efficiencies across all ports remain similar for the three devices, demonstrating that the design effectively reconfigures the on-chip distribution of the coupled energy without compromising the overall efficiency. These profiles demonstrate stable and efficient focusing characteristics across the target frequency band, thereby validating the broadband capability of the proposed devices.

2.5. Experimental Demonstrations

As proof-of-concept, we fabricated the devices (D1–D3) using conventional photolithography and metallization pro-

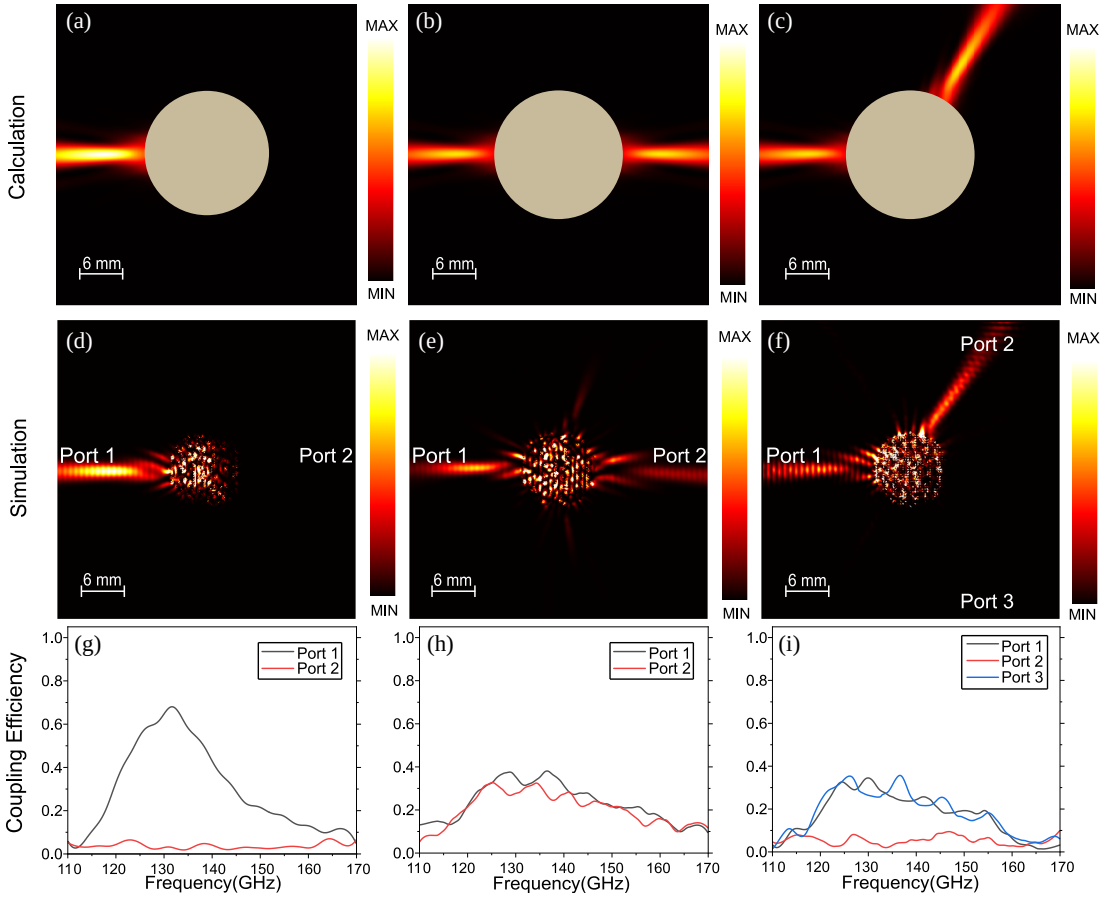

FIGURE 4. Theoretical and simulated focusing performance of the designed SW Couplers (D1–D3). (a)–(c) Theoretical electric field intensity distributions. A spatial mask is applied to mask the central singularity. (d)–(f) Simulated surface electric field distributions. (g)–(i) Simulated coupling efficiency of the proposed SW couplers. Identical Gaussian beam excitation parameters were maintained for all simulations to allow for a direct comparison.

cesses (details in Appendix Materials). Optical photographs (Figs. 5(a)–(c)) reveal well-defined metallic patterns, verifying the fabrication fidelity. For spectral characterization, an S-parameter measurement system was established (see Supplementary Note 3 for further details). To facilitate the efficient conversion from SWs to standard WR-6 waveguide modes, an adiabatic waveguide with a tapered transition was developed, and a QWP fabricated via 3D printing was integrated into the terahertz transmitter (see Supplementary Note 4 for details) [42]. Owing to the integration of these two non-standard custom components, standard Vector Network Analyzer (VNA) calibration and de-embedding procedures are insufficient to isolate their individual loss contributions. While the raw measured S-parameters encompass free-space path loss (FSPL), device-specific losses, and waveguide insertion losses, a reference-normalization procedure was implemented to isolate the system-induced effects. Specifically, a reference measurement was conducted by directly aligning two standard gain horn antennas at the same propagation distance.

The S-parameters presented in Figs. 5(d)–(f) are normalized against this reference, thereby specifically reflecting the coupling losses of the device and the insertion losses associated with the adiabatic transition and WR-6 waveguide. Despite the presence of these collective losses, the spectral characteristics exhibit remarkable agreement with the full-wave simulations (Figs. 4(g)–(i)) in terms of the resonant frequencies and bandwidths. Further analysis of Figs. 5(d)–(f) reveals that device D1 exhibits a 3 dB bandwidth of 18.55 GHz. Considering a 16-QAM modulation format with a peak efficiency of 4 bits per symbol, the measured bandwidths for D1 translate to minimum supported data rates of 74.19 Gbit/s. More competitively, for dual-channel devices, D2 achieved port bandwidths of 21.56 and 20.42 GHz, while D3 achieved bandwidths of 13.55 and 21.68 GHz. Owing to the high overlap of their center frequencies, the theoretical total transmission rates under the dual-link configuration reached 167.92 Gbit/s (D2) and 140.92 Gbit/s (D3). The bandwidth asymmetry in D3 originates from intensified crosstalk owing to the reduced channel spacing, which exacerbates the asymmetric coupling of surface waves. Furthermore, fabrication tolerances and slight setup misalignments further accentuate these performance discrepancies (see Supplementary Note 5 for details). Despite these practical variations, such high-speed transmission capabilities underscore the potential of these couplers as core components for next-generation, high-capacity terahertz wireless communication front-ends.

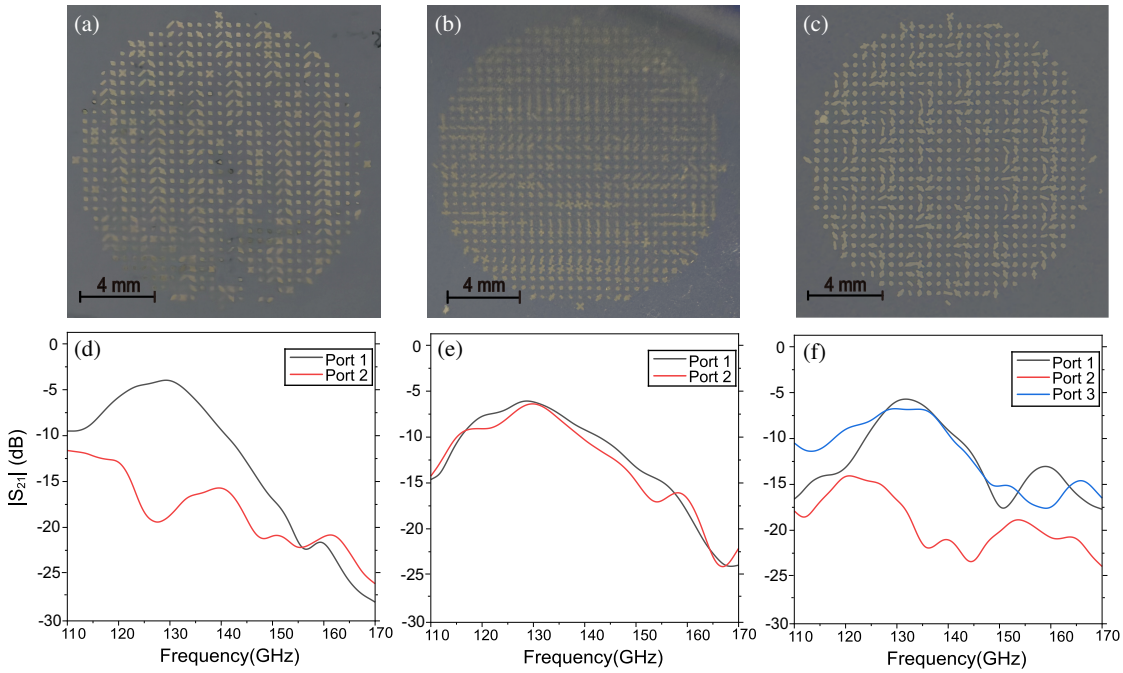

FIGURE 5. Experimental demonstration and performance characterization of the fabricated SW couplers. (a)–(c) Optical photographs of the fabricated samples (D1–D3) clearly display the central metasurface structures. (d)–(f) Measured S-parameters of the fabricated SW couplers.

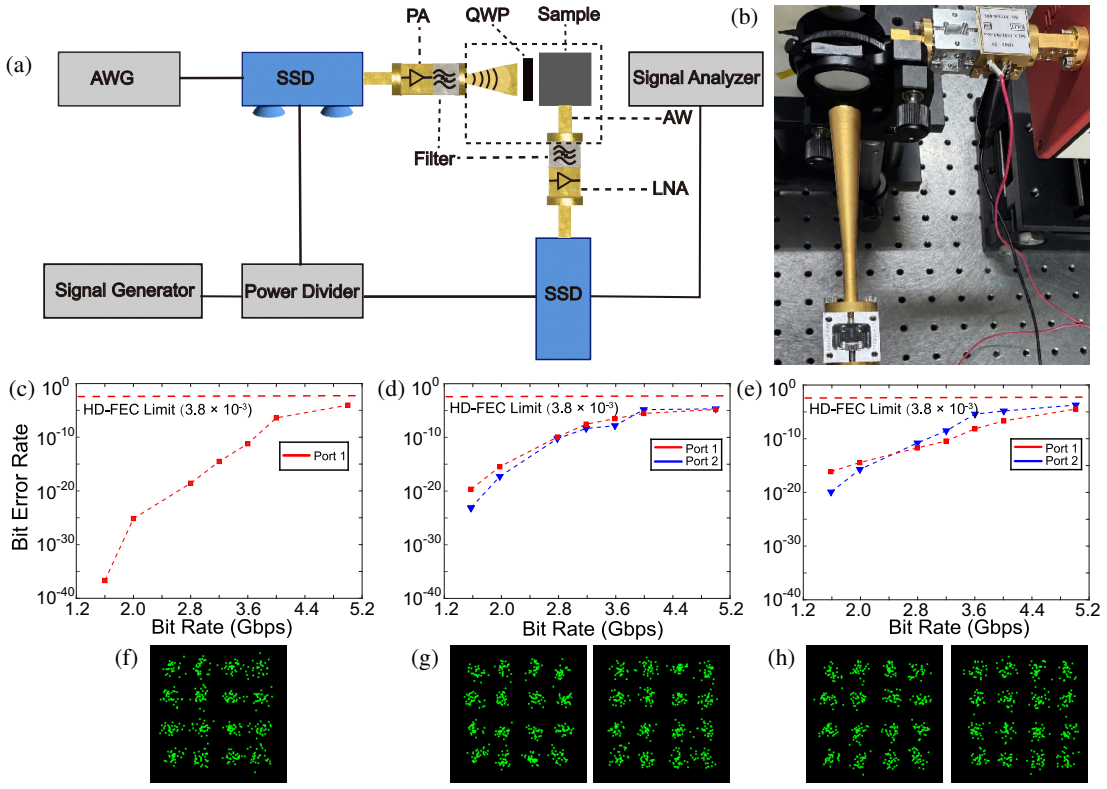

FIGURE 6. Experimental characterization of the fabricated Functional SW couplers. (a) Experimental setup for the terahertz free-space-to-chip communication link. (b) Photograph of the experimental system corresponding to the dashed box in (a). (c)–(e) Measured BER versus data rate for devices D1–D3. (f)–(h) Recovered 16-QAM constellation diagrams at 5 Gbit/s.

In addition, over the 130–150 GHz frequency range, the metasurfaces demonstrate robust channel selectivity. As derived from the S-parameter data shown in Figs. 5(d)–(f), the Isolation Ratio is calculated by averaging the values across the passband. Specifically, the ratio for D1 is measured at 8.17 dB, while for D3, the ratios reach 11.90 dB and 11.54 dB for the

TABLE 1. Comparison of the proposed SW coupler with other reported works.

Reference	Frequency	Efficiency	Wavefront-Control	Communication-Link
Jiang et al. [36, 37]	0.75 THz	3%–15%	✓	×
Duan et al. [31]	10 GHz	78%	×	×
Wang et al. [28]	0.4 THz	60%	✓	×
Liu et al. [38]	282 THz	35%	✓	×
This Work	0.14 THz	66.5%	✓	✓

respective orthogonal channels. These results indicate a high level of spatial discrimination, which is essential for suppressing inter-channel crosstalk and ensuring the signal-to-noise ratio (SNR) required for high-order modulation schemes, such as 16-QAM in the Terahertz regime.

To validate its communication performance, we established a dedicated link as illustrated in Figs. 6(a) and 6(b) to characterize high-speed data transmission (see Supplementary Note 3 for details). Overall, this represents a hybrid multi-physics link that bridges free-space waves, on-chip SWs, and guided modes.

To verify the signal quality and determine the maximum achievable transmission rate of the three fabricated devices, 16-QAM symbol sequences were transmitted at a center frequency of 133.2 GHz with a bandwidth of 1.25 GHz. The transmission quality was assessed via the bit error rate (BER), derived from the measured root-mean-square (RMS) error vector magnitude (EVM) using the following equation [43]:

$$\mathrm{BER} \approx \frac{2\left(1-\frac{1}{L}\right)}{\log_2 L} \cdot Q\left(\sqrt{\frac{3\log_2 L}{L^2-1} \cdot \frac{2}{\mathrm{EVM}_{\mathrm{RMS}}^2 \log_2 M}}\right). \quad (8)$$

where $M = 16$ and $L = \sqrt{M} = 4$ for the 16-QAM format. As illustrated in Figs. 6(c)–(e), the BER derived from Eq. (8) exhibits a gradual increase as the data rate rises from 1.6 to 5.0 Gbit/s. However, the values remained consistently below the hard decision forward error correction (HD-FEC) threshold of 3.8×10^{-3}. Consequently, all ports across the three devices successfully achieved a 16-QAM data transmission rate of 5 Gbit/s. Furthermore, Figs. 6(f)–(h) display the constellation diagrams for each port at 5 Gbit/s (corresponding to a symbol rate of 1.25 GBaud). The recovered 16-QAM constellations exhibited clear and well-separated clusters, indicating a high signal-to-noise ratio (SNR).

To rigorously quantify the efficiency enhancement underlying this performance, we adopted a comparative benchmarking approach (see Supplementary Note 6 for experimental data and test methods), evaluating the SW coupler against a geometric phase metallic strip coupler. This approach circumvents the challenge of calibrating the absolute system losses stemming from insertion, free-space propagation, and cascaded mode/polarization conversions. Under identical test conditions at 133.2 GHz, the metallic strip coupler yielded output powers of -26.74 and -34.29 dBm, whereas the proposed SW coupler achieved significantly higher outputs of -21.24 and -29.17 dBm. This yields a 3.55-fold efficiency enhancement, with comparable measured isolations of 7.55 and 7.93 dB, respectively.

3. CONCLUSION

In conclusion, we developed efficient and flexible SW couplers for the terahertz wireless communication receiver front ends. Full-wave simulations predict a coupling efficiency exceeding 60% over a 20 GHz bandwidth near 0.14 THz. As summarized in the performance comparison in Table 1, our proposed holographic SW coupler achieves a superior coupling efficiency of 66.5% at 140 GHz, significantly outperforming traditional geometric phase-based designs, which typically yield only 3%–15% efficiency. Beyond fundamental demonstrations, our device enables high-efficiency excitation, versatile on-chip routing, and a high-speed 16-QAM wireless communication link. These results underscore its potential as a robust platform for future 6G backhaul and on-chip interconnects. Although the absolute coupling efficiency is challenging to measure directly in the current system, the measured coupling efficiency significantly surpasses that of the geometric phase metallic strip couplers by a factor of 3.55. Moreover, the coupled SWs can be flexibly steered to the designated on-chip ports. Based on this design, 16-QAM terahertz wireless transmissions were demonstrated with superior BER and constellation results. Owing to the asymmetric electromagnetic paths and localized standing-wave modes within the structure, a slight distribution variance in group delay exists among different ports (see Supplementary Note 7). Nevertheless, reliable 16-QAM signal transmission was successfully demonstrated, with the measured BER performance well below the HD-FEC threshold. Further minimizing the group delay spread to support even higher data rates remains a promising direction for future research. In conjunction with recently reported multi/demultiplexing schemes, our couplers may serve as core components for enhancing the spectral efficiency of future terahertz wireless communications.

ACKNOWLEDGEMENT

This work was supported by the National Natural Science Foundation of China (Grant Nos. 62375203, 62335011, 62135008, 62535014, and U25A20512).

APPENDIX A. SAMPLE FABRICATION

All the samples in this study were fabricated using an identical process. First, AZ P4620 photoresist was spin-coated onto a 100-μm-thick, 2-inch silicon wafer. Following I-line ultraviolet (UV) exposure to transfer the photomask patterns, the wafer was developed in an NMD-W 2.38% developer to remove the photoresist from the exposed regions. Subsequently, an Induc-

tively Coupled Plasma (ICP) deep silicon etcher was employed to etch the silicon in these areas, thereby defining the specific wafer geometry required for insertion into the adiabatic waveguide.

Next, 200-nm-thick aluminum (Al) films were deposited onto both sides of the silicon wafer via magnetron sputtering. A layer of PR4000 photoresist was then spin-coated onto the top surface. After UV exposure to define the metallic structural patterns, the sample was developed using an RZX3038 solution to clear the exposed areas. In the subsequent step, the exposed Al layer was removed via wet etching using an acidic solution. Finally, the residual photoresist was stripped with acetone, followed by sequential rinsing with isopropanol and deionized (DI) water to eliminate any residues, yielding the final reflective metallic structures on the Si substrate.

APPENDIX B. NUMERICAL SIMULATIONS

In the simulations, aluminum was modeled as a lossy metal with a conductivity of $\sigma_{\mathrm{Al}} = 3.56 \times 10^7\ \mathrm{Sm}^{-1}$, while the silicon substrate was treated as a lossless dielectric with a permittivity of $\varepsilon_{\mathrm{Si}} \approx 11.9$. A time-domain solver was employed to characterize the electromagnetic response of the unit cells. Periodic boundary conditions were applied in the x- and y-directions, and open boundary conditions were imposed in the z-direction.

The excitation source, which generated 0.14 THz LCP wave that was normally incident onto the structure, was placed at $z = 20\,\mathrm{mm}$. An E-field probe was positioned 50 µm below the excitation source. Signal post-processing was performed on the time-domain probe data. We isolated the reflected signal by applying a time gate to suppress the incident waves. Subsequently, interpolation and a Fast Fourier Transform (FFT) were applied to the gated reflected signal to retrieve the amplitude and phase of the electric fields in the x- and y-directions. Because the designed meta-atoms function as quarter-wave plates to convert LCP waves into LP waves, we selected candidates exhibiting a high ratio of $|E_x|/|E_y|$ near 0.14 THz.

REFERENCES

[1] Dang, S., O. Amin, B. Shihada, and M.-S. Alouini, "What should 6G be?" *Nature Electronics*, Vol. 3, No. 1, 20–29, 2020.

[2] Nagatsuma, T., G. Ducournau, and C. C. Renaud, "Advances in terahertz communications accelerated by photonics," *Nature Photonics*, Vol. 10, No. 6, 371–379, 2016.

[3] Koenig, S., D. Lopez-Diaz, J. Antes, F. Boes, R. Henneberger, A. Leuther, A. Tessmann, R. Schmogrow, D. Hillerkuss, R. Palmer, *et al.*, "Wireless sub-THz communication system with high data rate," *Nature Photonics*, Vol. 7, No. 12, 977–981, 2013.

[4] Withayachumnankul, W., M. Fujita, and T. Nagatsuma, "Integrated silicon photonic crystals toward terahertz communications," *Advanced Optical Materials*, Vol. 6, No. 16, 1800401, 2018.

[5] Headland, D., A. K. Klein, M. Fujita, and T. Nagatsuma, "Dielectric slot-coupled half-Maxwell fisheye lens as octave-bandwidth beam expander for terahertz-range applications," *APL Photonics*, Vol. 6, No. 9, 096104, 2021.

[6] Gupta, M., N. Navaratna, P. Szriftgiser, G. Ducournau, and R. Singh, "327 Gbps THz silicon photonic interconnect with sub-λ bends," *Applied Physics Letters*, Vol. 123, No. 17, 171102, 2023.

[7] Headland, D., W. Withayachumnankul, M. Fujita, and T. Nagatsuma, "Gratingless integrated tunneling multiplexer for terahertz waves," *Optica*, Vol. 8, No. 5, 621–629, 2021.

[8] Gupta, M., A. Kumar, P. Pitchappa, Y. J. Tan, P. Szriftgiser, G. Ducournau, and R. Singh, "150 Gbps THz chipscale topological photonic diplexer," *Advanced Materials*, Vol. 36, No. 19, 2309497, 2024.

[9] Wang, W., Y. J. Tan, T. C. Tan, A. Kumar, P. Pitchappa, P. Szriftgiser, G. Ducournau, and R. Singh, "On-chip topological beamformer for multi-link terahertz 6G to XG wireless," *Nature*, Vol. 632, No. 8025, 522–527, 2024.

[10] Wang, W., Y. J. Tan, P. Szriftgiser, G. Ducournau, and R. Singh, "On-chip topological leaky-wave antenna for full-space terahertz wireless connectivity," *Nature Photonics*, Vol. 20, 317–323, 2026.

[11] Jia, R., S. Kumar, T. C. Tan, A. Kumar, Y. J. Tan, M. Gupta, P. Szriftgiser, A. Alphones, G. Ducournau, and R. Singh, "Valley-conserved topological integrated antenna for 100-Gbps THz 6G wireless," *Science Advances*, Vol. 9, No. 44, eadi8500, 2023.

[12] Xu, Z.-H., J. He, X. Hao, Y.-Q. Song, H. Ren, Q. Xu, J. Han, and S. Xu, "Quantitative terahertz communication evaluation of compact valley topological photonic crystal waveguides," *ACS Photonics*, Vol. 12, No. 4, 1822–1828, 2025.

[13] Wang, W.-Y., H. Ren, Z.-H. Xu, H. Chen, Y. Li, and S. Xu, "Integrated terahertz topological valley-locked power divider with arbitrary power ratios," *Optics Letters*, Vol. 49, No. 19, 5579–5582, 2024.

[14] Ren, H., S. Xu, Z. Lyu, Y. Li, Z. Yang, Q. Xu, Y.-S. Yu, Y. Li, F. Gao, X. Yu, J. Han, Q.-D. Chen, and H.-B. Sun, "Terahertz flexible multiplexing chip enabled by synthetic topological phase transitions," *National Science Review*, Vol. 11, No. 8, nwae116, 2024.

[15] Yang, Y., Y. Yamagami, X. Yu, P. Pitchappa, J. Webber, B. Zhang, M. Fujita, T. Nagatsuma, and R. Singh, "Terahertz topological photonics for on-chip communication," *Nature Photonics*, Vol. 14, No. 7, 446–451, 2020.

[16] Digiorgio, V., U. Senica, P. Micheletti, M. Beck, J. Faist, and G. Scalari, "On-chip, inverse-designed active wavelength division multiplexer at THz frequencies," *Nature Communications*, Vol. 16, No. 1, 7711, 2025.

[17] Chong, F., Y. Wu, B. Gao, S. Li, H. Chen, and S. Han, "Inverse-designed on-chip terahertz three-channel mode and wavelength division demultiplexer," *Advanced Photonics Research*, Vol. 7, No. 2, e202500250, 2026.

[18] Herter, A., A. Shams-Ansari, M. Lončar, and J. Faist, "Thin-film lithium niobate terahertz differential field detectors with a bandwidth reaching 3 Terahertz," *Nature Communications*, Vol. 16, No. 1, 8864, 2025.

[19] Blatter, T., S. M. Koepfli, A. Zuerrer, S. Hess, Y. Horst, M. Destraz, D. Rieben, M. Baumann, L. Kulmer, J. Smajic, Y. Fedoryshyn, and J. Leuthold, "All-plasmonic sub-terahertz wireless communication link," *Nature Communications*, Vol. 16, No. 1, 9988, 2025.

[20] Zhang, Y., J. Yang, Y. Zeng, Z. Chen, H. Feng, S. Zhu, K.-M. Shum, C. H. Chan, and C. Wang, "Monolithic lithium niobate photonic chip for efficient terahertz-optic modulation and terahertz generation," *Nature Communications*, Vol. 16, No. 1, 10330, 2025.

[21] Cameron, T. R. and G. V. Eleftheriades, "Experimental validation of a wideband metasurface for wide-angle scanning leaky-wave antennas," *IEEE Transactions on Antennas and Propaga-*

tion, Vol. 65, No. 10, 5245–5256, 2017.

[22] Li, W., J. Chen, S. Gao, L. Niu, J. Wei, R. Sun, Y. Wei, W. Tang, and T. J. Cui, "An externally perceivable smart leaky-wave antenna based on spoof surface plasmon polaritons," *Opto-Electronic Advances*, Vol. 7, No. 9, 240040, 2024.

[23] Yao, D., P. H. He, H. C. Zhang, J. Zhu, M. Hu, and T.-J. Cui, "Miniaturized photonic and microwave integrated circuits based on surface plasmon polaritons," *Progress In Electromagnetics Research*, Vol. 175, 105–125, 2022.

[24] Liu, C., Y. Li, F. Huang, G. Xu, Q. Li, S. Wang, Q. Xu, J. Gu, and J. Han, "Dual non-diffractive beam generation via spin-and-frequency multiplexed all-dielectric metasurfaces," *Progress In Electromagnetics Research*, Vol. 181, 21–33, 2024.

[25] Hao, H., X. Ran, Y. Tang, S. Zheng, and W. Ruan, "A single-layer focusing metasurface based on induced magnetism," *Progress In Electromagnetics Research*, Vol. 172, 77–88, 2021.

[26] Zhang, X., Q. Xu, L. Xia, Y. Li, J. Gu, Z. Tian, C. Ouyang, J. Han, and W. Zhang, "Terahertz surface plasmonic waves: A review," *Advanced Photonics*, Vol. 2, No. 1, 014001, 2020.

[27] Xu, Q., Y. Lang, X. Jiang, X. Yuan, Y. Xu, J. Gu, Z. Tian, C. Ouyang, X. Zhang, J. Han, and W. Zhang, "Meta-optics inspired surface plasmon devices," *Photonics Insights*, Vol. 2, No. 1, R02, 2023.

[28] Wang, Z., S. Li, X. Zhang, X. Feng, Q. Wang, J. Han, Q. He, W. Zhang, S. Sun, and L. Zhou, "Excite spoof surface plasmons with tailored wavefronts using high-efficiency terahertz metasurfaces," *Advanced Science*, Vol. 7, No. 19, 2000982, 2020.

[29] Huang, L., X. Chen, B. Bai, Q. Tan, G. Jin, T. Zentgraf, and S. Zhang, "Helicity dependent directional surface plasmon polariton excitation using a metasurface with interfacial phase discontinuity," *Light: Science & Applications*, Vol. 2, No. 3, e70, 2013.

[30] Pors, A., M. G. Nielsen, T. Bernardin, J.-C. Weeber, and S. I. Bozhevolnyi, "Efficient unidirectional polarization-controlled excitation of surface plasmon polaritons," *Light: Science & Applications*, Vol. 3, No. 8, e197, 2014.

[31] Duan, J., H. Guo, S. Dong, T. Cai, W. Luo, Z. Liang, Q. He, L. Zhou, and S. Sun, "High-efficiency chirality-modulated spoof surface plasmon meta-coupler," *Scientific Reports*, Vol. 7, No. 1, 1354, 2017.

[32] Lang, Y., Q. Xu, G. Xu, X. Zhang, Q. Li, and J. Han, "Topological metasurface for spin-decoupled wavefront manipulation of terahertz surface plasmons," *Laser & Photonics Reviews*, Vol. 19, No. 4, 2401281, 2025.

[33] Yuan, X., Q. Xu, Y. Lang, Z. Yao, X. Jiang, Y. Li, X. Zhang, J. Han, and W. Zhang, "Temporally deuterogenic plasmonic vortices," *Nanophotonics*, Vol. 13, No. 6, 955–963, 2024.

[34] Yuan, X., Q. Xu, Y. Lang, X. Jiang, Y. Xu, X. Chen, J. Han, X. Zhang, J. Han, and W. Zhang, "Tailoring spatiotemporal dynamics of plasmonic vortices," *Opto-Electronic Advances*, Vol. 6, No. 4, 220133, 2022.

[35] Lang, Y., Q. Xu, X. Chen, J. Han, X. Jiang, Y. Xu, M. Kang, X. Zhang, A. Alù, J. Han, and W. Zhang, "On-chip plasmonic vortex interferometers," *Laser & Photonics Reviews*, Vol. 16, No. 10, 2200242, 2022.

[36] Jiang, X., W. Liu, Q. Xu, Y. Lang, Y. Fu, F. Huang, H. Dai, Y. Li, X. Zhang, J. Gu, J. Han, and W. Zhang, "On-chip terahertz orbital angular momentum demultiplexer," *Photonics Research*, Vol. 12, No. 5, 1044–1054, 2024.

[37] Jiang, X., Q. Xu, Y. Lang, W. Liu, X. Chen, Y. Xu, H. Ren, X. Wang, S. Xu, X. Zhang, *et al.*, "Geometric phase control of surface plasmons by dipole sources," *Laser & Photonics Reviews*, Vol. 17, No. 6, 2200948, 2023.

[38] Liu, F., D. Wang, H. Zhu, X. Zhang, T. Liu, S. Sun, X. Zhang, Q. He, and L. Zhou, "High-efficiency metasurface-based surface-plasmon lenses," *Laser & Photonics Reviews*, Vol. 17, No. 7, 2201001, 2023.

[39] Bliokh, K. Y., F. J. Rodríguez-Fortuño, F. Nori, and A. V. Zayats, "Spin-orbit interactions of light," *Nature Photonics*, Vol. 9, No. 12, 796–808, 2015.

[40] Bliokh, K. Y., Y. Gorodetski, V. Kleiner, and E. Hasman, "Coriolis effect in optics: Unified geometric phase and spin-Hall effect," *Physical Review Letters*, Vol. 101, No. 3, 030404, 2008.

[41] Bliokh, K. Y., "Geometrical optics of beams with vortices: Berry phase and orbital angular momentum Hall effect," *Physical Review Letters*, Vol. 97, No. 4, 043901, 2006.

[42] Fu, Y., T. Ye, W. Tang, and T. Chu, "Efficient adiabatic silicon-on-insulator waveguide taper," *Photonics Research*, Vol. 2, No. 3, A41–A44, 2014.

[43] Shafik, R. A., M. S. Rahman, and A. R. Islam, "On the extended relationships among EVM, BER and SNR as performance metrics," in *2006 International Conference on Electrical and Computer Engineering*, 408–411, Dhaka, Bangladesh, 2006.